Received: 2 March 2020 | Revised: 6 April 2020 | Accepted: 26 April 2020

DOI: 10.1002/aoc.5807

FULL PAPER

Applied Organometallic Chemistry WILEY

Synthesis, physico-chemical characterization and bioevaluation of Ni(II), Pd(II), and Pt(II) complexes with 1-(*o*-tolyl)biguanide: Antimicrobial and antitumor studies

Ileana Nuţă[1] | Mihaela Badea[1] | Mariana Carmen Chifiriuc[2,3] | Coralia Bleotu[4] | Marcela Popa[2] | Constantin-Gabriel Daniliuc[5] | Rodica Olar[1]

[1]Faculty of Chemistry, University of Bucharest, 90-92 Panduri Str., Bucharest, 050663, Romania

[2]Faculty of Biology, University of Bucharest, 1-3 Aleea Portocalelor Str., Bucharest, 60101, Romania

[3]Life, Environment and Earth Sciences Department, Spl. Independentei 91-95, Research Institute of the University of Bucharest, Bucharest, Romania

[4]Stefan S Nicolau Institute of Virology, 285 Mihai Bravu Ave, Bucharest, Romania

[5]Organisch-Chemisches Institut, Westfälische Wilhelms-Universität Münster, Corrensstrasse 40, Münster, 48149, Germany

Correspondence
Rodica Olar, University of Bucharest, Faculty of Chemistry, 90-92 Panduri Str., 050663 Bucharest, Romania.
Email: rodica_m_olar@yahoo.com

New complexes of type $[M(tbg)_2]Cl_2$ [tbg = 1-(*o*-tolyl)biguanide; M = Ni(II), Pd(II), and Pt(II)] were synthesized and characterized to develop new biologically active compounds. The features of the complexes were assigned from microanalytical and thermal data. The NMR, FT-IR, and UV-Vis spectra were established by comparison with HtbgCl. All complexes exhibit a square-planar geometry resulting from the chelating behavior of tbg. The HtbgCl and $[Ni(tbg)_2]Cl_2$ complexes were fully characterized by single-crystal X-ray diffraction. The HtbgCl species crystallize in the monoclinic *C*2/*c* spatial group, while the Ni(II) complex adopts an orthorhombic $Pna2_1$ spatial group. The structure is stabilized by a complex hydrogen bonds network. The *in vitro* antimicrobial assays revealed improved antimicrobial activity for complexes in comparison with the ligand against both planktonic and biofilm embedded microbial cells. The most efficient compound, showing the largest spectrum of antimicrobial activity, including Gram-positive and Gram-negative bacteria, as well as fungal strains, in both planktonic and biofilm growth states was the Pd(II) complex, followed by the Pt(II) complex. The Pt(II) compound exhibited the most significant antiproliferative activity on the human cervical cancer SiHa cell line, inducing a cell cycle arrest in the G2/M phase.

KEYWORDS

complex, 1-(*o*-tolyl)biguanide, antimicrobial activity, biofilm, human cervical cancer

1 | INTRODUCTION

Antimicrobial drug resistance has become one of the greatest public health challenges at the global level for the twenty-first century, highlighting the urgent need for the discovery of new antibacterial agents.[1–7]

One of the strategies used for developing new and effective antimicrobial agents is the enhancement of organic species activity by complexation. Such studies have indicated promising antimicrobial potential for complexes bearing a chelate ligand and/or a species that exhibits anti-adhesive abilities.[8–10]

Interest in the field of biguanides has been raised by evidence of the good antibiofilm activity of 1,1′-(1,3-phenylene)bis (biguanide)[11] and the antimicrobial activity shown by complexes with such derivatives both on planktonic and biofilm embedded strains.[8,12–20]

Among these, Cu(II),[8,12,13] Mn(II),[13] and Zn(II)[12,14] complexes with *N*,*N*′-dimethylbiguanide (dmbg) have been found to be efficient against planktonic

Gram-positive and Gram-negative bacteria. Moreover, species of Mn(II), Ni(II), Cu(II), and Zn(II) with this ligand showed the ability to inhibit *Staphylococcus aureus* and *Pseudomonas aeruginosa* biofilm development on an inert substratum.[12,13] Significant inhibitory activity was observed for Fe(III)[15] and Pd(II)[16] complexes with dmbg against both planktonic and biofilm embedded cells of *S. aureus*, *Bacillus subtilis*, and *Escherichia coli*. The Pd(II) complex showed antibiofilm activity against *Candida albicans*,[16] while Cu(II) complexes with 1-(*o*-tolyl)biguanide (tbg) against *S. aureus* and *P. aeruginosa* biofilms.[17]

As for complexes with mixed ligands, Cu(II), Fe(III), Mn(III),[14] and Ni(II)[15] species with α-ketoglutarate anion and tbg exhibited good antibiofilm activity against *S. aureus* and *P. aeruginosa* strains. Also, organoiridium(III) species with cyclopentadienyl and biguanide derivatives proved to be active against a large spectrum of microbial strains, including the methicillin-resistant *S. aureus* (MRSA), and were also able to disrupt and eradicate bacterial mature biofilm.[20]

Furthermore, for Ni(II) complexes with dmbg either the ability to cleave DNA[21] or cytotoxicity against HepG2 human liver cancer[22] was evidenced.

The biological activity of biguanide complexes is not surprising since, after coordination, the biguanide scaffold can engage a large variety of noncovalent interactions with biological targets, such as hydrogen bonds, dipole–dipole, lone pair (N)–π and π–π stacking, rendering it a powerful pharmacophore. Some of these interactions have been evidenced for several complexes in their supramolecular arrangement in solid networks.[8,20,23] The possible interactions for tbg complexes are presented in Figure 1.

Moreover, both antimicrobial and antiproliferative activities for Ni(II),[24–26] Pd(II),[27–31] and Pt(II)[30,31] complexes with Schiff bases, species bearing the same imine donor groups such biguanides, have recently been reported.

Bearing these points in mind, we report here the synthesis of Ni(II), Pd(II), and Pt(II) chloride complexes with tbg. The compounds were characterized by elemental and thermal analyses, NMR, FT-IR, and UV–visible (UV-Vis) spectra. The HtbgCl and Ni(II) complexes were fully characterized through single-crystal X-ray diffraction.

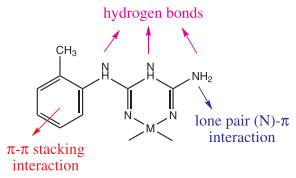

FIGURE 1 Non-covalent interactions posible for 1-(o-tolyl) biguanide complexes

Bioevaluation of the antimicrobial activity of the compounds was performed on a large variety of bacterial and fungal strains, in both planktonic and biofilm states. The antiproliferative activity was tested on the human cervical cancer SiHa cell line by CellTiter Glo and cell cycle analysis.

2 | EXPERIMENTAL

2.1 | Materials and reagents

The high-purity reagents were purchased from Sigma-Aldrich (Saint-Louis, MO, USA) ($NiCl_2 \cdot 6H_2O$, tbg) and Fluka (Saint-Louis, MO, USA) ($PdCl_2$, $PtCl_2$) and were used as received, without further purification.

2.2 | Physical measurements

Chemical analysis of carbon, nitrogen, and hydrogen was performed on a Perkin Elmer (Waltham, MA, USA) PE 2400 analyzer. FT-IR spectra were recorded in KBr pellets with a Bruker (Billerica, MA, USA) Tensor 37 spectrometer in the range 400–4000 cm^{-1}. ^1H NMR and ^{13}C NMR spectra were recorded on a Bruker Fourier spectrometer (working frequency 300 MHz) at 25°C. Chemical shifts were measured in parts per million from internal standard tetramethylsilane (TMS). Electronic spectra were established by the diffuse reflectance technique, using spectralon as standard and were recorded in the range 200–1500 nm, on a Jasco (Easton, MD, USA) V670 spectrophotometer. The heating curves (thermogravinetric (TG), derivative thermogravimetric (DTG) and differential thermal analysis (DTA)) were recorded using a Labsys 1200 SETARAM (Caluire, France) instrument, with a sample mass of 7–12 mg over a temperature range of 20–900°C, using a heating rate of 10°C/min. The measurements were carried out in a synthetic air atmosphere (flow rate 17 cm^3/min) using alumina crucibles. The X-ray powder diffraction patterns were collected on a DRON-3 (St. Petersburg, Russia) diffractometer with nickel-filtered Cu K_α radiation (λ = 1.5418 Å) in a 2θ range of 5 70°, step width 0.05°, and an acquisition time of 2 s per step. X-ray single-crystal diffraction data sets were collected with a Nonius Kappa (Delft, The Netherlands) CCD diffractometer. Programs used: data collection COLLECT,[32] data reduction Denzo-SMN,[33] absorption correction Denzo,[34] structure solution *SHELXT*-2015,[35] structure refinement *SHELXL*-2015,[36] and graphics *XP*.[37] *R* values are given for observed

reflections and wR^2 values are given for all reflections. Crystallographic data for HtbgCl and $[Ni(tbg)_2]Cl_2$ structures have been deposited with the Cambridge Crystallographic Data Centre, CCDC Nos. 1904301 and 1904302, respectively. Copies of the data can be obtained free of charge.

2.3 | Synthesis and analytical data of tbg hydrochloride and complexes

The tbg hydrochloride (HtbgCl) was synthesized by adding 1 mL of 37% HCl solution to a solution containing 1 mmol (191 mg) of tbg in 20 mL of ethanol. The obtained solution was heated under magnetic stirring for 2 hr. Single crystals suitable for X-ray diffraction were obtained after slow evaporation of this solution.

$[Ni(tbg)_2]Cl_2$ (**1**): A solution of 382 mg (2 mmol) tbg in 40 mL of ethanol was dropwise added to a solution containing 237 mg (1 mmol) nickel(II) chloride hexahydrate in 20 mL of ethanol. The reaction mixture was refluxed for 2 hr until the color changed to orange. The sparingly soluble species was obtained after cooling the solution at room temperature and the volume was reduced to half by slow evaporation. The resulting solid product was filtered off, washed with hot ethanol and diethyl ether, and dried at room temperature. Single crystals suitable for X-ray diffraction were obtained by the slow diffusion of the tbg ethanol solution in nickel(II) chloride ethanol solution: yield 464 mg (91%); analysis found: C 42.32, H 5.03, N 27.44; $NiC_{18}H_{26}N_{10}Cl_2$ requires: C 42.22, H 5.12, N 27.35%.

The other complexes of the series were obtained by the same method starting from $PdCl_2$ and $PtCl_2$, respectively.

$[Pd(tbg)_2]Cl_2$ (**2**): yield 412 mg (74%); analysis found: C 38.67, H 4.61, N 25.11; $PdC_{18}H_{26}N_{10}Cl_2$ requires: C 38.62, H 4.68, N 25.02%.

$[Pt(tbg)_2]Cl_2$ (**3**): yield 524 mg (81%); analysis found: C 42.32, H 5.03, N 27.44; $PtC_{18}H_{26}N_{10}Cl_2$ requires: C 33.34, H 4.04, N 21.60%.

2.4 | Antimicrobial assays

The antimicrobial activity of the obtained compounds was determined on bacterial and fungal reference strains (*Escherichia coli* ATCC 25922, *Pseudomonas aeruginosa* ATCC 27853, *Staphylococcus aureus* ATCC 29213, *Bacillus subtilis* ATCC 6633, *Enterococcus faecalis* ATCC 29212, *Candida albicans* 22). The quantitative antimicrobial activity assay was performed by the liquid broth microdilution method, allowing to establish the minimal inhibitory concentration (MIC), as previously reported.[38,39] The antibiofilm activity assay was performed by the violet crystal microtiter method, establishing of the minimal biofilm eradication concentration (MBEC), following previously described protocols.[38,39] All biological experiments were performed in triplicate.

2.5 | In vitro cytotoxicity assays

2.5.1 | Cell culture conditions

The human cervical cancer SiHa cell line (ATCC HTB-35) was cultivated in DMEM:F12 (GE Life Sciences, Pittsburgh, USA) supplemented with 10% heat-inactivated bovine serum and penicillin/streptomycin at 37°C with 5% CO_2.

2.5.2 | Cell viability

The CellTiter-Glo luminescent cell viability assay (Promega, Madison, WI, USA) was used to quantify the adenosine triphosphate (ATP) generated by metabolically active cells. The cells were seeded at a concentration of 10^4 cell per well in 96-well plates. The compounds were added in triplicate at concentrations ranging between 400 and 50 μg/ml. The plates were then incubated for 24 hr and the cells were lysed using 100 μl of CellTiter-Glo reagent for 10 min at room temperature. The luminescence was recorded in a TriStar luminometer (Berthold Technologies GmbH & Co.KG, BW, Bad Wildbad, Germany). The cell viability was calculated as the percentage of viable cells from the sample reported to the total number of cells of control.

The fluorescein diacetate (FDA) and propidium iodide (PI) dual stain was used as the second method for toxicity confirmation.[40] Briefly, the cellular monolayer obtained in each 24-well plate was treated with 100 μg/ml of the tested compounds. After 24 hr, 10 μg/ml of FDA and 20 μg/ml of PI were added and the stained cells were evaluated with an Observer D1 Zeiss fluorescence microscope (Zeiss GmbH, Gottingen, Germany).

2.5.3 | Cell cycle analysis

For the cell cycle analysis, the monolayer obtained from 10^5 cells was treated with 100 μg/ml of the tested compounds for 24 hr at 37°C in 5% CO_2 atmosphere and humid conditions. The cells were harvested using trypsin:EDTA (Sigma-Aldrich, Saint-Louis, MO, USA), washed in phosphate saline buffer (PBS), fixed in 70%

ethanol, and maintained at −20°C overnight. Rehydrated sample were treated with 100 μg/ml RNAse A and 10 μg/ml propidium iodide (Sigma) and incubated at 37°C for 1 hr. An Epics XL Beckman Coulter flow cytometer (Beckman Coulter, Indianapolis, IN, USA) was used for sample acquisition and FlowJo 7.2.5 software (FlowJo, LLC, Ashland, OR, USA) was used for cell cycle analysis.

3 | RESULTS AND DISCUSSION

3.1 | Synthesis and physicochemical characterization of ligand and complexes

Nickel(II), palladium(II), and platinum(II) complexes with tbg were obtained from refluxing an ethanol solution of ligand and the metal(II) (M: Ni, Pd, Pt) chloride in a 1:2 molar ratio as depicted in Scheme 1.

The elemental (experimental part) and thermal analysis data confirmed the 1:2 metal to ligand stoichiometry for all complexes. The compounds were formulated as mononuclear species based on single-crystal X-ray diffraction as well as NMR, FT-IR, and UV-Vis spectra.

3.1.1 | Description of tbg hydrochloride and $[Ni(tbg)_2]Cl_2$ structure

The details of the crystal parameters, data collection, and refinement for complexes are summarized in Table 1. The compound tbg hydrochloride crystallized in the monoclinic crystal system *C*2/*c* with an ionic structure containing the protonated tbg unit and the corresponding chloride anion in the asymmetric unit cell (Figure 2a and Supporting Information Figure S1). The packing diagram of HtbgCl compound presents a complex hydrogen bonds network. Dimeric units are built between two cationic units involving N–H··· N hydrogen bonds (N2–H03··· N3 2.993(2) Å and 167(2)° (Figure 2b and Supporting Information Figure S2)). An additional six N–H··· Cl hydrogen bonds found between the cationic and anionic units (Supporting Information Table S1 and Figure S3) lead to the formation of a polymeric chain parallel to the *ab* plane (Figure 2c, and Supporting Information Figures S4 and S5). No relevant π··· π interactions were found between the aromatic substituents.

The $[Ni(tbg)_2]Cl_2$ complex crystallizes in the orthorhombic space group $Pna2_1$ with four molecules in the unit cell (Figure 3a and Supporting Information Figure S6). In addition to the classical hydrogen bonds interactions (N–H··· Cl) (Supporting Information Table S2 and Figure S7) noncovalent intermolecular π··· π interactions between the biguanide units and the adjacent *o*-tolyl substituents were observed in the packing diagram (Figure 3b and Supporting Information Figure S8). The combination of these two types of interactions leads to the formation of a three-dimensional network with a zigzag arrangement of cationic complex units (Figure 3c and Supporting Information Figure S9).

TABLE 1 Summary of crystal data for HtbgCl and $[Ni(tbg)_2]Cl_2$ (**1**)

Compound	Htbg	$[Ni(tbg)_2]Cl_2$ (1)
Color/shape	Colorless/plate	Orange/plate
Empirical formula	$C_9H_{14}ClN_5$	$C_{18}H_{26}Cl_2N_{10}Ni$
Formula weight	227.70	512.10
Temperature	223(2) K	223(2) K
Crystal system	Monoclinic	Orthorhombic
Space group	*C*2/c	$Pna2_1$
Unit cell dimensions	a = 18.5936(5) Å	a = 14.3504(7) Å
	b = 13.8288(3) Å	b = 8.0550(3) Å
	c = 9.3332(3) Å	c = 19.7390(9) Å
	β = 99.097(1)°	a = 14.3504(7) Å
Volume	2369.63(11) $Å^3$	2281.68(17) $Å^3$
Z	8	4
Calculated density	1.277 mg/m^3	1.491 mg/m^3
Absorption coefficient	0.300 mm^{-1}	3.612 mm^{-1}
F(000)	960	1064
Goodness-of-fit on F^2	1.099	1.016
Final R indices [$I > 2\sigma(I)$]	$R1$ = 0.0434	$R1$ = 0.0458
	$wR2$ = 0.0978	$wR2$ = 0.1111
R indices (all data)	$R1$ = 0.0508	$R1$ = 0.0526
	$wR2$ = 0.1045	$wR2$ = 0.1171
Largest difference peak and hole	0.193 and −0.241 e $Å^{-3}$	0.407 and −0.213 e $Å^{-3}$

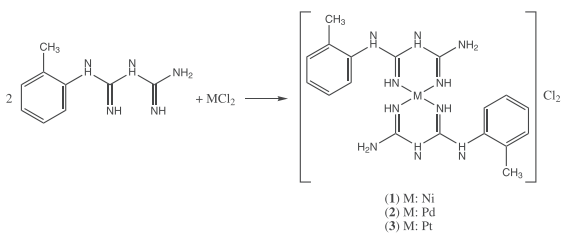

SCHEME 1 Complexes synthesis procedure

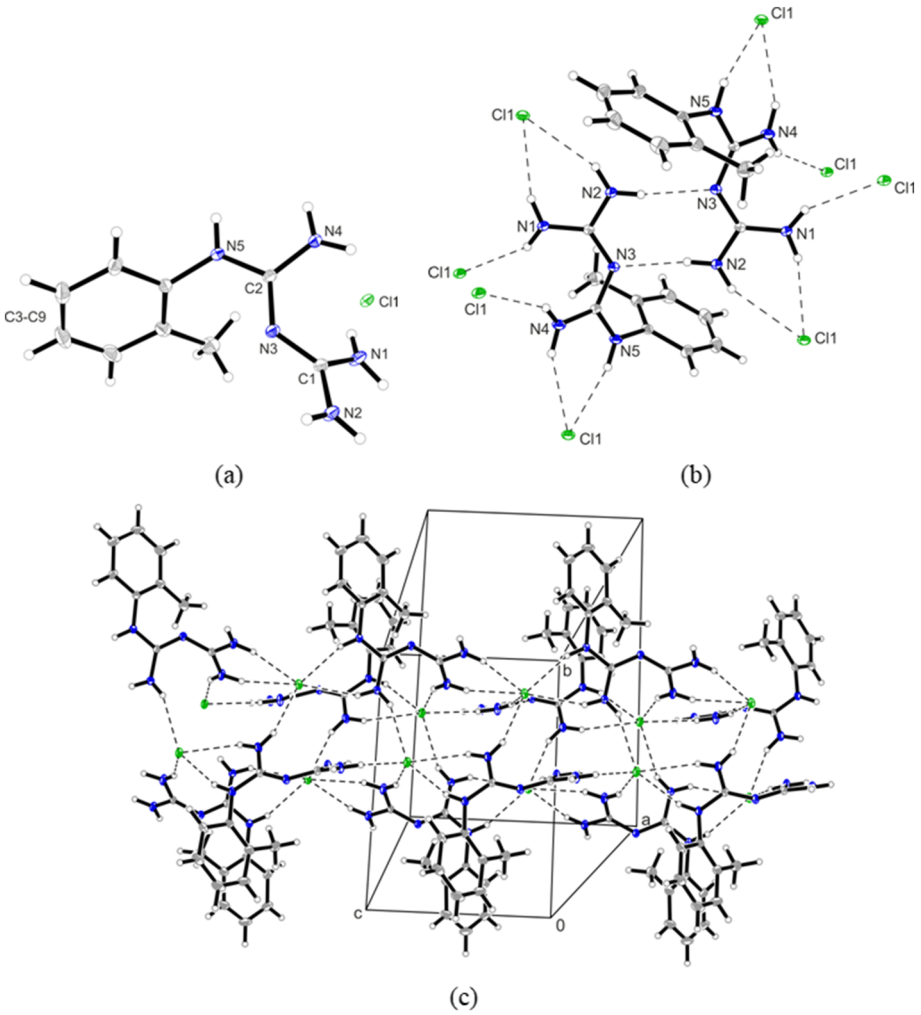

FIGURE 2 Asymmetric unit of HtbgCl (thermal ellipsoids at the 15% probability level) (a), dimmer type formation involving N-H···N interactions between the cationic units (b) and excerpt of the packing diagram representing the formation of a polymeric chain parallel to the ab-plane (c)

3.1.2 | FT-IR and NMR spectral data

The IR selected bands of tbg and complexes are listed in Table 2. The spectra of tbg and HtbgCl are similar, with only small differences in the characteristic range of amine group vibrations. The band assigned to the imine moiety stretching vibration ν(C=NH) appears at 1612 cm^{-1} in the spectrum of tbg and is shifted to lower wavenumbers by 2–7 cm^{-1} in the complexes spectra. This modification indicates the involvement of the imine groups in coordination.[17]

A new weak band appears in the range 1300–1305 cm^{-1} in the complexes spectra; according to the available literature data this band can be assigned to the vibration of the six-membered chelate ring formed by metallic ion coordination at two imine groups from a biguanide molecule.[41]

The system composed by three bands in the range 3310–3350 cm^{-1}, assigned to asymmetrical and symmetrical stretching vibrations of the NH_2 group, as well as to stretching vibration of NH groups, is shifted in the spectra of the complexes to lower wavenumbers. Moreover, the band assigned to NH_2 group deformation is shifted by 5–10 cm^{-1} in the same direction. All these aspects result from tbg coordination and thus from the hydrogen bond rearrangement in the solid network as otherwise was shown for Ni(II) complex.

The shifting of the bands assigned to the *o*-substituted aromatic ring to lower wavenumbers is the result of both charge density reorganization in the tbg molecule after coordination and $\pi^{\cdots}$ π interactions.

The tbg presence in the complexes structure was confirmed by the ^{1}H NMR and ^{13}C NMR spectra patterns. In the ^{1}H NMR spectrum of tbg the singlet at 2.13 ppm assigned to methyl protons is downfield shifted, a shift that increases with the increasing polarizing action of the metallic ion. The signals of phenyl ring protons appear as multiplets at 6.84 and 7.13 ppm and are both upfield and downfield shifted as result of neighborhood modification after coordination (Table 3). It is well known that chemical shifts of NH protons can occur virtually anywhere in ^{1}H NMR spectra.[42] Since for tbg and its combinations the signals of imine and amine groups are not observed, this

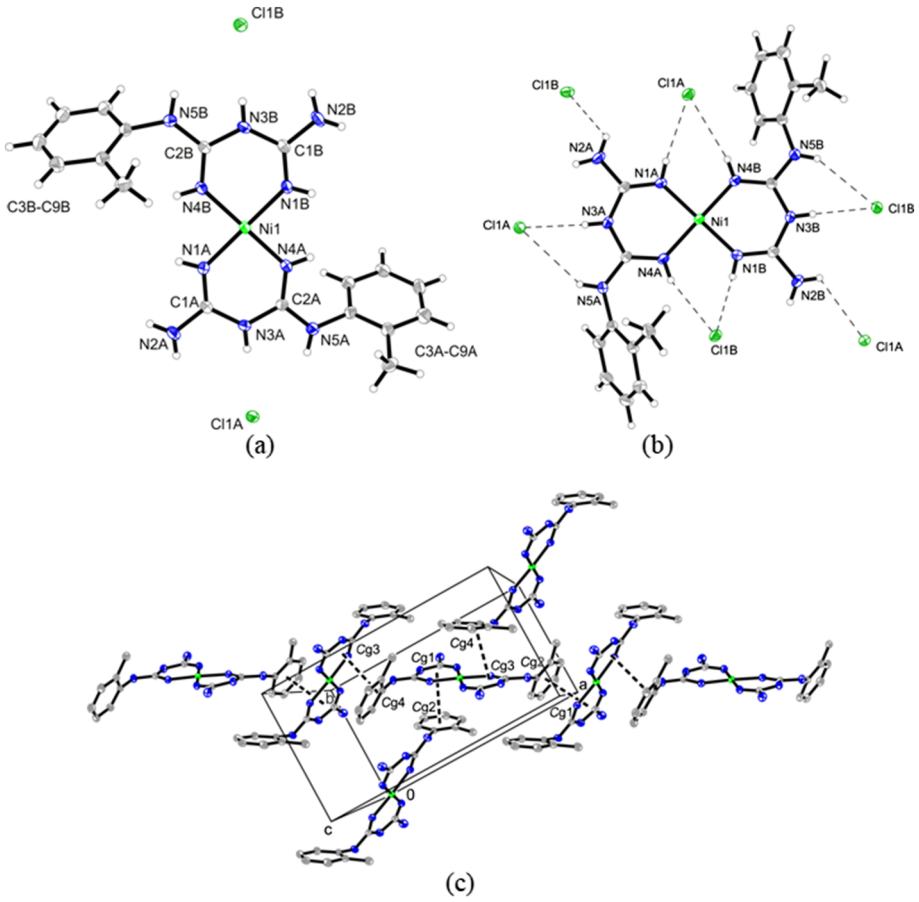

FIGURE 3 Asymmetric unit of complex (**1**) (thermal ellipsoids at the 15% probability level) (a), hydrogen interaction N-H···Cl between the cations and anions (b) and intermolecular p···p interactions between the biguanide units and adjacent o-tolyl substituents (c)

TABLE 2 Absorption maxima (cm^{-1}) from FT-IR spectra and assignments for tbg, its hydrochloride, and complexes **1**–**3**

tbg	HtbgCl	1	2	3	Assignments
3464 m	3470 m	3352 s	3344 s	3344 m	$\nu_{asym}(NH_2)$
3434 m	3434 m	3348 m	3333 m	3328 m	$\nu_{sym}(NH_2)$
3376 m	3377 m	3312 m	3319 m	3321 m	$\nu(NH)$
	3356 m				
3108 m	3110 w	3069 m	3061 m	3075 m	$\nu(CH)_{aromatic}$
2906 w	2960 w	2961 m	2920 w	2961 m	$\nu_{as}(CH_3)$
2815 w	2891 w	2832 w	2856 w	2898 w	$\nu_{s}(CH_3)$
1612 vs	1612 vs	1605 vs	1608 vs	1610 vs	$\nu(C{=}N)$
1525 s	1578 s	1517 vs	1535 vs	1520 vs	$\delta(NH_2)$
1482 m	1483 s	1486 m	1482 s	1495m	$\nu(C{=}C)_{aromatic}$
–	–	1301 w	1305 w	1305 w	ν(chelate ring)
1248 m	1250 m	1265 m	1256 m	1261 m	$\nu(C_{aromatic}{-}N)$
1115 w	1116 w	1100 w	1105 w	1114 w	$\nu(C_{aliphatic}{-}N)$
749 m	750 m	721 m	727 m	746 w	$\gamma(CH)_{aromatic}$

Note. vs, very strong; s, strong; m, medium; w, weak; sym, symmetrical; asym, asymmetrical.

indicates that they appear in the same region as the aromatic ones and thus are hidden. The ^{13}C NMR spectra show the signal characteristic for a methyl group at 39.7 ppm while those for aromatic carbon atoms appear in the range 127-152 ppm, depending on the neighboring atoms. The signal assigned to imine carbon atoms is upfield shifted by 4–5 ppm as result of coordination of nitrogen atoms of this group.

TABLE 3 The shifts in ^{1}H and ^{13}C NMR spectra of tbg, HtbgCl, and complexes

	δ (ppm)							
Compound	CH_3	CH	CH	C=NH	CH_3	CH	CH–CH_3	CH–NH
tbg/HtbgCl	2.13	6.84	7.13	18.1	39.5	126.6 130.4	150.7	151.7
$[Ni(tbg)_2]Cl_2$ (**1**)	2.14	6.67	7.20	17.6	39.7	127.3 131.4	150.6	151.6
$[Pd(tbg)_2]Cl_2$ (**2**)	2.17	6.71	7.25	17.7	39.7	127.6 131.6	150.2	151.7
$[Pt(tbg)_2]Cl_2$ (**3**)	2.22	6.78	7.25	17.7	39.7	127.5 131.6	150.2	151.6

3.1.3 | UV-vis spectra

Solid state UV-Vis spectra provided useful information concerning the stereochemistry for d^8 ions. In both tbg and HtbgCl spectra one band assigned to intraligand $\pi \rightarrow \pi^*$ transitions appears at about 34,500 cm^{-1}. This band is shifted to higher energy in the spectra of the complexes as result of coordination (Supporting Information Figure S10).

The electronic spectra of all complexes show the pattern of the square-planar geometry with the band assigned to spin allowed transition $^{1}A_{1g} \rightarrow {}^{1}A_{2g}$.[43] This band is located at 22,990 cm^{-1} for complex **1**, 26,315 cm^{-1} for complex **2**, and 28,990 cm^{-1} for complex **3** accordingly to the splitting parameter increase in series $3d^8 < 4d^8 < 5d^8$.

3.1.4 | Thermal behavior of complexes

Thermal analyses data (TG, DTG, and DTA) were used to obtain information concerning the thermal stability of the complexes. The thermal decomposition data are summarized in Table 4 and are discussed in the following paragraphs.

The curves corresponding to complex **1** indicate that decomposition follows three well-defined steps (Figure 4). The sharp and intense endothermic signal

TABLE 4 Thermal behavior data (in air) for complexes

Compound	Step	Thermal effect	Temperature range/ °C	Δm_{exp} (%)	Δm_{calc} (%)	Process
$[Ni(tbg)_2]Cl_2$ (**1**)	1	Endothermic	206	–	–	Melting
	2	Miscellaneous	206–420	31.9	31.8	Chloride elimination and oxidative degradation of 24% tbg
	3	Exothermic	420–700	43.3	41.5	Oxidative degradation of 56% tbg
	4	Exothermic	700–900	11.4	12.1	Oxidative degradation of 20% tbg and NiO formation
		Residue		**14.4**	**14.6**	
$[Pd(tbg)_2]Cl_2$ (**2**)	1	Endothermic	200–380	38.3	38.0	Chloride and 37% tbg elimination
	2	Exothermic	380–830	42.8	43.0	Oxidative degradation of 63% tbg
		Residue		**18.9**	**19.0**	
$[Pt(tbg)_2]Cl_2$ (**3**)	1	Endothermic	158–290	5.5	5.6	Chloride elimination
	2	Endothermic	290–395	14.1	13.9	Chloride elimination and oxidative degradation of 15% tbg
	3.	Exothermic	395–740	47.8	47.9	Oxidative degradation of 85% tbg and PtO formation
	4	Exothermic	800–860	2.3	2.5	PtO decomposition
		Residue		**30.1**	**30.1**	

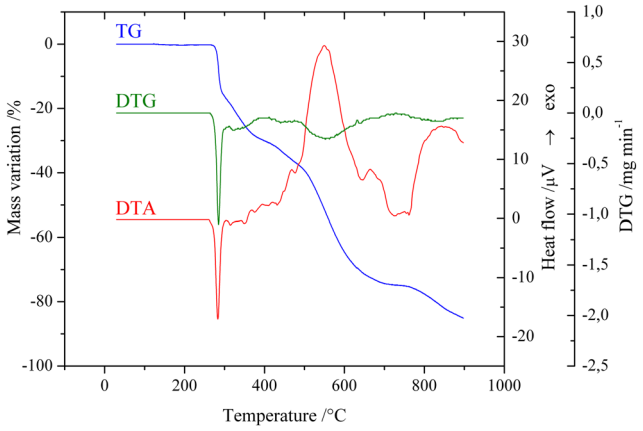

FIGURE 4 TG, DTG and DTA curves of $[Ni(tbg)_2]Cl_2$ (**1**)

seen at the beginning of decomposition indicates the complex melting point at 206°C. The DTA curve shows one endothermic event for the first step that with a mass loss of 31.9% (calcd 31.8%) corresponds to chloride anions together with NH=C–NH_2 group elimination from each tbg molecule. The decomposition continues with oxidative degradation of the $CH_3C_6H_4NH$ moieties, accompanied by a mass loss of 43.3% (calcd 41.5%). On the DTA curve in the 420–700°C range several overlapping exothermic processes can be observed, one of them being very strong. This strong effect is due to the aromatic moiety burning. In the last step NiO formation occurs together with further tbg oxidative degradation. The overall mass loss of 85.6% fits well with the calculated one of 85.4%.

Complex **2** is also anhydrous and thus stable up to 175°C. As result of higher molar weight both Pd(II) and Pt(II) complexes decompose without melting. The decomposition starts with the elimination of chlorine anions and of CH_2 and N=C(N)–NH_2 tbg fragments (Supporting Information Figure S11), processes accompanied by 38.3% (calcd 38.0%) mass loss and several endothermic effects. The endothermic effect is the result of the bond-breaking process predominating over reorganization. According to the DTA curve at least two overlapping exothermic processes occur until the Pd is formed at 830°C (found/calcd overall mass loss: 81.1/81.0%).

Complex **3** decomposition starts with elimination of one chloride anion according with the mass loss of 5.5% (calcd 5.6%), a process accompanied by a weak endothermic effect (Supporting Information Figure S12). The second step is another chloride anion elimination, a process that overlaps with the elimination of both methyl and amine groups from tbg. These processes lead to a mass loss of 14.1% (calcd 13.9%). The oxidative degradation of the rest of the tbg starts immediately, accompanied by several strong exothermic effects and a mass loss of 47.8% (calcd 47.9%). The decomposition continues with PtO decomposition that leads to Pt as residue at 860°C (found/calcd overall mass loss: 69.9/69.9%). PtO, similar to PdO, is a covalent species that decomposes in air with metal formation.[44]

3.2 | Antimicrobial activity assay

3.2.1 | Antimicrobial efficiency of the complexes against planktonic cells

The antimicrobial activity of the tested compounds against planktonic microbial cells is summarized in Table 5. It can be noticed that complexes **2** and **3** present superior antimicrobial activity against all tested strains in the planktonic state, with MIC values 2 to 64 times lower than those of tbg and between 2 and 128 times lower than those of HtbgCl. Complexes **2** and **3** exhibited exceptional antibacterial activity against the *P. aeruginosa* strain, which is well known for its intrinsic and acquired multiple drug-resistance mechanisms, thus showing very promising potential for the development of novel tools for fighting antimicrobial resistance. Complex **3**showed better antibacterial activity against the two Gram-negative strains (i.e., *E. coli* and *P. aeruginosa*), while

TABLE 5 MIC and MBEC (μg/ml) values of the tbg, HtbgCl, and complexes 1–3 against microbial strains in planktonic growth form

	tbg		HtbgCl		1		2		3	
Strain	**MIC**	**MBEC**	**MIC**	**MBEC**	**MIC**	**MBEC**	**MIC**	**MBEC**	**MIC**	**MBEC**
E. coli	>1000	1000	>1000	>1000	>1000	1000	500	15.62	62.5	62.5
P. aeruginosa	500	500	1000	>1000	125	125	15.62	15.62	7.81	7.81
S. aureus	500	500	>1000	>1000	>1000	7.81	62.5	62.5	125	125
B. subtilis	500	500	>1000	>1000	500	62.5	31.25	31.25	125	125
E. faecalis	>1000	1000	>1000	>1000	125	125	125	125	125	125
C. albicans	>1000	>1000	1000	>1000	>1000	>1000	62.5	62.5	125	125

complex **2** exhibited a larger antimicrobial spectrum, with low MIC values ranging from 15.62 to 62.5 μg/ml against four of the six tested microbial strains. Complex **1** showed improved antimicrobial activity compared to tbg and HtbgCl for only two bacterial strains, *P. aeruginosa* and *E. faecalis*, respectively.

A possible mechanism for the antimicrobial activity of the obtained complexes is their ability to penetrate the microbial cell wall and to interact and inactivate intracellular targets (proteins or DNA). Considering the ionic nature of these species, their cytosolic internalization can occur not only by passive diffusion mediated by the *o*-tolyl moiety, but also by using organic cation transporters. Thus, the good activity noticed for Pd(II) and Pt(II) complexes could be related to their affinity for such molecules. Bearing in mind that the investigated complexes have the same oxidation state and configuration of metallic ion, coordination geometry, N_4 donor set, chelate effect, and counterion, the differences in the intensity of the antimicrobial activity of the complexes can be only related to complex cation dimension.

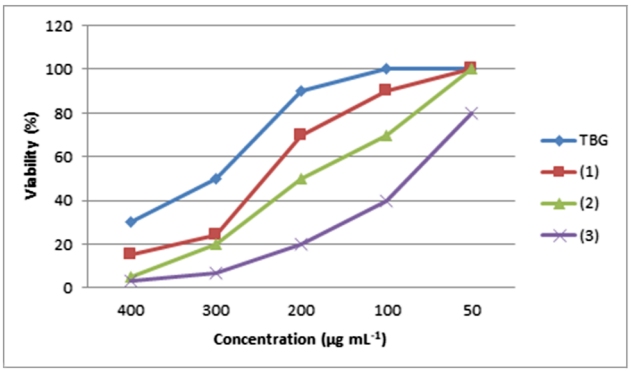

FIGURE 5 Assessment of cytotoxicity of tested compounds by using CellTiter Glo

3.2.2 | Antibiofilm activity of the complexes

Biofilm development amplifies the antimicrobial resistance phenomenon and 70–80% of all infections are produced by microbial biofilms.[45,46] Moreover, due to the

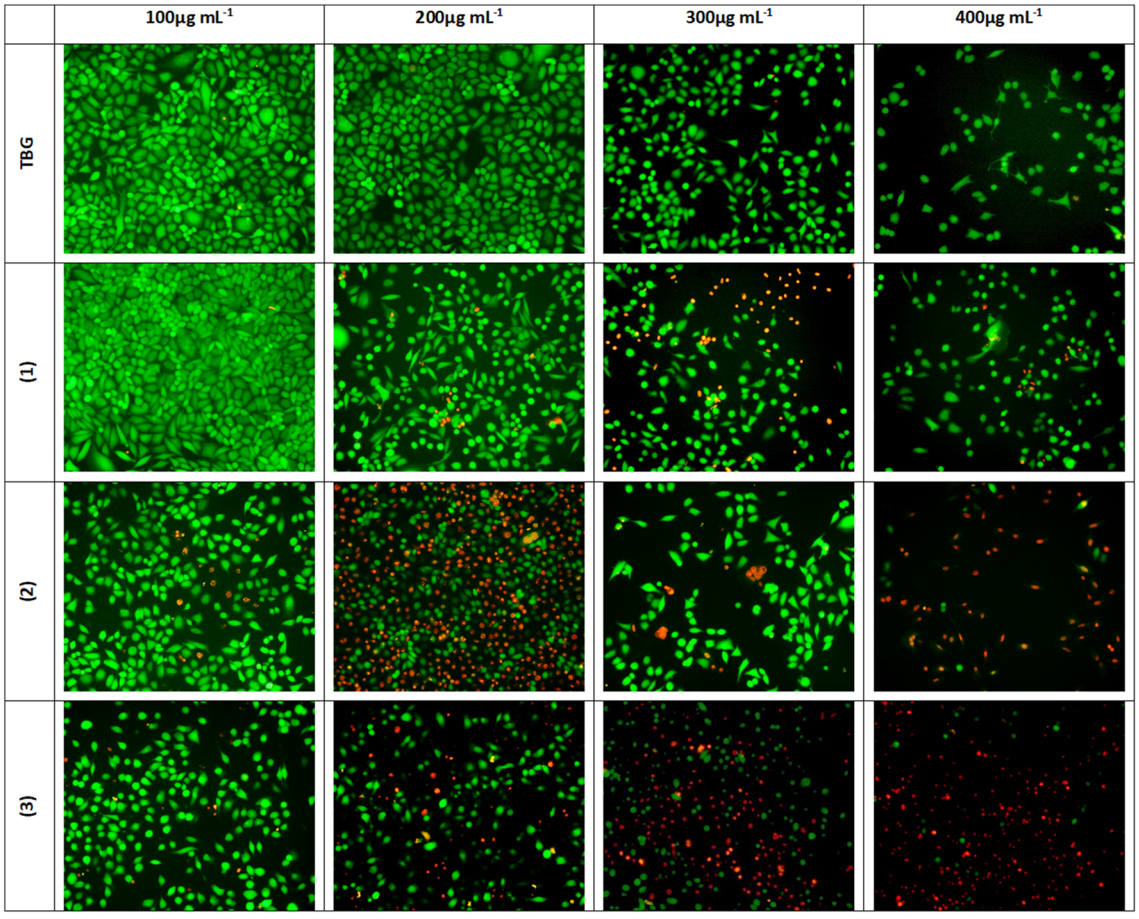

FIGURE 6 The cell viability observed using FDA/PI stain (Propidium iodide, the double-stranded DNA dye, cross the plasma membrane of compromised/permeabilized cells. Stained altered cells can be observed in red in fluorescent microscopy. Fluorescein diacetate, a cell-permeant esterase substrate, cross the plasma membrane of viable cells. The integrity of cell-membrane is required for intracellular retention of the product associated with green stain in fluorescent microscopy.)

high density and close proximity of bacterial cells inside biofilms, the horizontal gene transfer of resistance genes is facilitated in different habitats.[47] Taking into account the important contribution of microbial biofilms to the global threat of antimicrobial resistance, a huge research effort is presently dedicated to the development of antibiofilm strategies.[38] The antibiofilm activity of the tested complexes proved to be much improved compared to that of the tbg and HtbgCl precursors for all complexes, with two exceptions for complex **1** in the case of *E. coli* and *C. albicans* biofilms. Remarkably, complexes **2** and **3** preserved the same efficiency against planktonic and biofilm-embedded *P. aeruginosa* cells, as revealed by the similar values of MIC and MBEC. Also, complex **1**shows better efficiency against the biofilm embedded *S. aureus* and *B. subtilis* cells, in comparison with the planktonic growth state, the MBEC being 8 to 128 times lower than the corresponding MIC values. The same behavior was seen for complex **2** and *E. coli* biofilm, with an MBEC value 32 times lower than the corresponding MIC one.

3.2.3 | Cytotoxicity assays

To establish IC_{50}, the cytotoxic activity of the compounds was tested using CellTiter Glo (Figure 5) and confirmed by fluorescence microscopy using FDA/PI staining (Figure 6). It has been observed that TBG and compound **1** exhibit a low toxicity with IC_{50} values of 270.18 and 226.84 μg/ml, respectively. In contrast, the most cytotoxic compound was **3**, with an IC_{50} of 59.52 μg/ml. This value is higher in comparison with those reported in the scientific literature for cisplatin (IC_{50} 8.47 μg/ml), but similar to that of carboplatin (IC_{50} 39.44 μg/ml).[48]

3.2.4 | Cell cycle analysis

The cytotoxicity data were also confirmed by cell cycle analysis. The appearance of the sub-G0 fraction peak on the left of the G1 peak demonstrates the occurrence of apoptotic cells (Figure 7). At a concentration of 100 μg/ml tbg induced a slight increase of the G1 fraction and a decrease in the S fraction. As seen in Figure 8, compound **3** exhibited the most intensive pro-apoptotic effect at a concentration of 100 μg/ml, where the sub-G0 peak was very high. This aspect is very important considering that this type of tumor cell develops resistance to cisplatin and its analogues. Because the species $[Pt(tbg)_2]Cl_2$, have a different stability, these could probably exhibit a different metabolization pathways and/or a different mechanism of action different metabolization pathways and exhibit a different mechanism of action. At a concentration of 50 μg/ml, compound **3** induced a cell cycle arrest in G2/M. This effect is probably due to the presence of

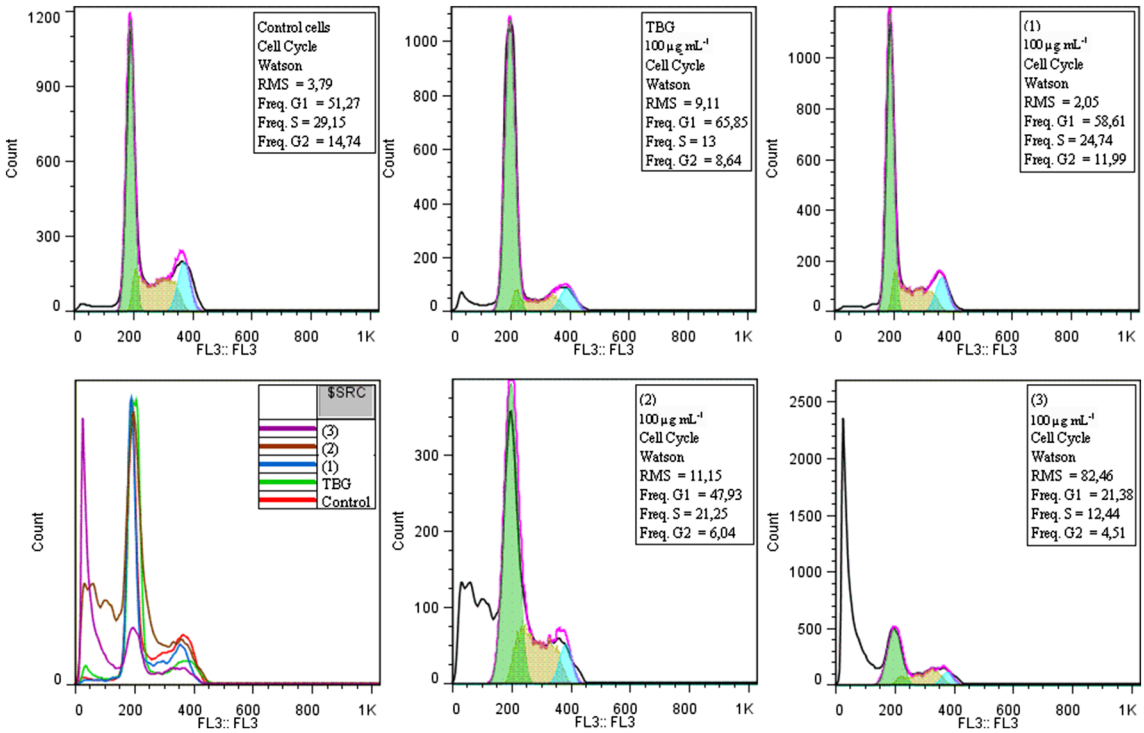

FIGURE 7 The effect induced by the treatment with 100 μg mL-1 on the cell cycle (Data are expressed as fractions of cells in the different cell cycle phases.)

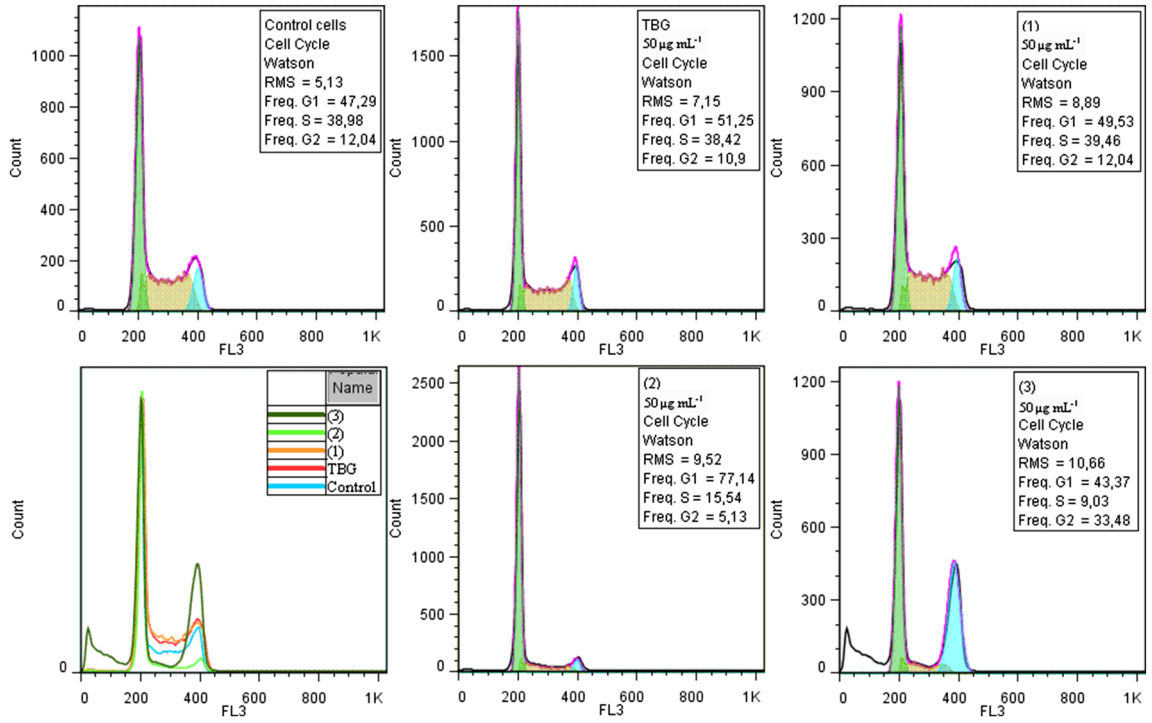

FIGURE 8 The effect induced by the treatment with 50 µg mL-1 on the cell cycle (Data were expressed as fractions of cells in the different cell cycle phases.)

Pt(II) as it is known that compounds with this ion are blockers of the G2/M phase.[49,50]

4 | CONCLUSION

Direct reaction of metal chloride with tbg allowed the synthesis of new complexes $[M(tbg)_2]Cl_2$ (M: Ni, Pd, Pt), which were further submitted to physicochemical characterization. The FT-IR spectra displayed the characteristic features of the biguanide derivatives acting as chelate through imine nitrogen atoms. The complexes displayed square planar stereochemistry in accordance with the UV-Vis spectra features.

Complexes were stable up to 150–200°C as result of their anhydrous nature. Decomposition started with hydrochloric acid elimination followed by tbg fragmentation and oxidative degradation.

Taken together, the results of the antimicrobial assays performed on bacterial and fungal strains in both the planktonic and biofilm growth states revealed improved antimicrobial activity of the complexes compared to the ligand. The efficiency of the complexes was similar or even better against microbial biofilms, which are known for their higher resistance to a large spectrum of inhibitory agents, therefore these complexes are very promising for the development of novel antibiofilm agents. The most efficient complex, showing the largest spectrum of antimicrobial activity, including Gram-positive and Gram-negative bacteria, as well as fungal strains, in both planktonic and biofilm growth states, was complex **2**, followed by complex **3**.

The toxicity of the tested compounds on the SiHa cancer line increased in the following order: tbg < **1** <**2** < **3**. The ability of **3** to induce cycle arrest in the G2/M phase is important for its further development as a potential antitumor agent.

ORCID

Mihaela Badea https://orcid.org/0000-0002-4018-7610
Rodica Olar https://orcid.org/0000-0002-4208-0972

REFERENCES

[1] R. J. Guidos, *Clin. Infect. Dis.* **2011**, *52*, S397.
[2] F. Corona, J. L. Martinez, *Antibiotics (Basel)* **2013**, *2*, 237.
[3] R. Wise, *J. Antimicrob. Chemother.* **2011**, *66*, 1939.
[4] M. Blaser, O. Carrs, G. Cassell, N. Fishman, R. Guidos, S. Levy, J. Powers, R. Norrby, G. Tillotson, *J. Antimicrob. Chemother.* **2011**, *66*, 1941.
[5] T. M. Belete, *Human Microbiome J.* **2019**, *11*, 100052.
[6] M. V. Dias-Souza, C. G. Dias, P. H. Ferreira-Marçal, *Biointerface Res Appl Chem* **2018**, *8*, 3259.
[7] L. D. R. Dos Santos, A. E. S. Dos Santos, I. P. Cerávolo, F. J. B. Figueiredo, M. V. Dias-Souza, *Biointerface Res Appl Chem* **2018**, *8*, 3565.
[8] R. Olar, M. Badea, D. Marinescu, C. M. Chifiriuc, C. Bleontu, M. N. Grecu, E. E. Iorgulescu, M. Bucur, V. Lazăr, A. Finaru, *Eur. J. Med. Chem.* **2010**, *45*, 2868.

[9] S. Siabi, H. Pasdar, N. Foroughifar, M. Davallo, R. Fazaeli, *Bio-interface Res Appl Chem* **2018**, *8*, 3418.
[10] M. G. Abuelazm, O. A. El-Gammal, S. A. Mandour, *Bio-interface Res Appl Chem* **2019**, *9*, 4547.
[11] T. Böttcher, I. Kolodkin-Gal, R. Kolter, R. Losick, J. Clardy, *J. Am. Chem. Soc.* **2013**, *135*, 2927.
[12] R. Olar, M. Badea, M. N. Grecu, D. Marinescu, V. Lazar, C. Balotescu, *J. Therm. Anal. Calorim.* **2008**, *92*, 239.
[13] R. Olar, M. Badea, D. Marinescu, M. Chifiriuc, C. Bleotu, M. N. Grecu, E. Iorgulescu, V. Lazar, *Eur. J. Med. Chem.* **2010**, *45*, 3027.
[14] R. Olar, M. Badea, E. Cristurean, V. Lazar, R. Cernat, C. Balotescu, *J. Therm. Anal. Calorim.* **2005**, *80*, 451.
[15] M. Badea, A.-M. Crasanda, M. C. Chifiriuc, L. Marutescu, V. Lazar, D. Marinescu, R. Olar, *J. Therm. Anal. Calorim.* **2013**, *111*, 1743.
[16] M. Badea, E. Iosub, C. M. Chifiriuc, L. Marutescu, E. E. Iorgulescu, V. Lazar, D. Marinescu, C. Bleotu, R. Olar, *J. Therm. Anal. Calorim.* **2013**, *111*, 1753.
[17] R. Olar, M. Badea, D. Marinescu, E. E. Iorgulescu, E. Frunza, V. Lazar, C. Chifiriuc, *J. Therm. Anal. Calorim.* **2010**, *99*, 815.
[18] M. Mihalache, O. Oprea, B. Ş. Vasile, C. Guran, I. L. Ardelean, *UPB Sci. Bull. B Chem. Mat. Sci.* **2018**, *80*, 113.
[19] M. Mihalache, O. Oprea, C. Guran, I. L. Ardelean, *C. R. Chim.* **2018**, *21*, 32.
[20] F. Chen, J. Moat, D. McFeely, G. Clarkson, I. J. Hands-Portman, J. P. Furner-Pardoe, F. Harrison, C. G. Dowson, P. J. Sadler, *J. Med. Chem.* **2018**, *61*, 7330.
[21] K. Rajeshwari, P. Vasantha, B. S. Kumar, B. Shekhar, P. V. A. Lakshmi, *Appl. Organomet. Chem.* **2019**, *33*, e5351.
[22] F. I. Elshami, A. E. M. M. Ramadan, M. M. Ibrahim, I. M. El-Mehasseb, S. Al-Juaid, S. Y. Shaban, *Appl. Organomet. Chem.* **2019**, *33*, e5437.
[23] P. Hubberstey, U. Suksangpanya, *Struct. Bonding* **2004**, *111*, 46.
[24] M. Gaber, K. El-Baradie, N. El-Wakiel, S. Hafez, *Appl. Organomet. Chem.* **2019**, *33*, e5348.
[25] I. Babahan, A. Özmen, M. Aksel, M. D. Bilgin, R. Gumusada, M. E. Gunay, F. Eyduran, *Appl. Organomet. Chem.* **2020**, *34*, e5632.
[26] W. H. Mahmoud, M. M. Omar, Y. M. Ahmed, G. G. Mohamed, *Appl. Organomet. Chem.* **2020**, *34*, e5528.
[27] L. H. Abdel-Rahman, M. S. S. Adam, A. M. Abu-Dief, H. Moustafa, M. T. Basha, A. S. Aboraia, B. S. Al-Farhan, H. El-Sayed Ahmed, *Appl. Organomet. Chem.* **2018**, e4527.
[28] A. M. Abu-Dief, L. H. Abdel-Rahman, A. A. Hassan Abdel-Mawgoud, *Appl. Organomet. Chem.* **2019**, *33*, e5373.
[29] S. A. Elsayed, H. M. El-Gharabawy, I. S. Butler, F. M. Atlam, *Appl. Organomet. Chem.* **2020**, *34*, e5643.
[30] M. Gaber, H. A. El-Ghamry, S. K. Fathalla, *Spectrochim. Acta a Mol. Biomol. Spectrosc.* **2015**, *139*, 396.
[31] M. Gaber, H. A. El-Ghamry, M. A. Mansour, *J. Photochem. Photobiol. A Chem.* **2018**, *354*, 163.
[32] R. W. W. Hooft, B. V. Nonius, *COLLECT, Program for Collecting Data on CCD Area Detectors*, Delft, The Netherlands **1998**.
[33] Z. Otwinowski, W. Minor, *Methods Enzymol.* **1997**, *276*, 307.
[34] Z. Otwinowski, D. Borek, W. Majewski, W. Minor, *Acta Crystallogr.* **2003**, *A59*, 228.
[35] G. M. Sheldrick, *Acta Crystallogr.* **2015**, *A71*, 3.
[36] G. M. Sheldrick, *Acta Crystallogr.* **2015**, *C71*, 3.
[37] XP, *Interactive molecular graphics, Version 5.1*, Bruker AXS Inc., Madison, Wisconsin, USA **1998**.
[38] C. Chifiriuc, V. Lazăr, C. Bleotu, I. Călugărescu, A. M. Grumezescu, D. E. Mihaiescu, D. E. Mogoşanu, A. S. Buteică, E. Buteică, *Digest J. Nanomat. Biostruct.* **2011**, *6*, 37.
[39] I. D. Vlaicu, R. Olar, C. Maxim, M. C. Chifiriuc, C. Bleotu, N. Stănică, G. Vasile Scăeţeanu, C. Dulea, S. Avram, M. Badea, *Appl. Organomet. Chem.* **2019**, *33*, e4976.
[40] A. T. Bordei Telehoiu, D. C. Nuţă, M. T. Căproiu, F. Dumitrascu, I. Zarafu, P. Ioniţă, C. D. Bădiceanu, S. Avram, M. C. Chifiriuc, C. Bleotu, C. Limban, *Molecules* **2020**, *25*, 266.
[41] P. V. Babykutty, C. P. Prabhakaran, R. Anantaraman, C. G. R. Nair, *J. Inorg. Nucl. Chem.* **1974**, *36*, 3685.
[42] M. H. Abraham, R. J. Abraham, W. E. Acree, A. E. Aliev, A. J. Leo, W. L. Whaley, *J. Org. Chem.* **2014**, *79*, 11075.
[43] E. I. Solomon, A. B. P. Lever, Inorganic Electronic Structure and Spectroscopy, Vol. II, in *Applications and Case Studies*, John Wiley & Sons, New York, Chichester, Weinheim, Brisbane, Singapore, Toronto **2006**.
[44] P. Štarha, Z. Trávníček, I. Popa, *J. Inorg. Biochem.* **2009**, *103*, 978.
[45] Z. Khatoon, C. D. McTiernan, E. J. Suuronen, T. F. Mah, E. I. Alarcon, *Heliyon* **2018**, *4*, e01067.
[46] M. M. Mihai, A. M. Holban, C. Giurcăneanu, L. G. Popa, M. Buzea, M. Filipov, V. Lazăr, M. C. Chifiriuc, M. I. Popa, *Rom. J. Morphol. Embryol.* **2014**, *55*, 1401.
[47] T. Stalder, E. Top, *NPJ Biofilms Microbiomes* **2016**, *2*, 16022.
[48] P. Khumkhrong, K. Piboonprai, W. Chaichompoo, W. Pimtong, M. Khongkow, K. Namdee, A. Jantimaporn, D. Japrung, U. Asawapirom, A. Suksamrarn, T. Iempridee, *Biomolecules* **2019**, *9*, 494.
[49] S. William-Faltaos, D. Rouillard, P. Lechat, G. Bastian, *Fundam. Clin. Pharmacol.* **2007**, *21*, 165.
[50] W. Zheng, Z. Luo, J. Zhang, P. Min, W. Li, D. Xu, Z. Zhang, P. Xiong, H. Liang, J. Liu, *Mol. Med. Rep.* **2017**, *15*, 2795.

SUPPORTING INFORMATION

Additional supporting information may be found online in the Supporting Information section at the end of this article.

How to cite this article: Nuţă I, Badea M, Chifiriuc MC, et al. Synthesis, physico-chemical characterization and bioevaluation of Ni(II), Pd(II), and Pt(II) complexes with 1-(*o*-tolyl)biguanide: Antimicrobial and antitumor studies. *Appl Organomet Chem*. 2020;e5807. https://doi.org/10.1002/aoc.5807